Journal of Magnetism and Magnetic Materials 511 (2020) 166947

Contents lists available at ScienceDirect

Journal of Magnetism and Magnetic Materials

journal homepage: www.elsevier.com/locate/jmmm

Research articles

Round robin comparison on quantitative nanometer scale magnetic field measurements by magnetic force microscopy

Xiukun Hu[a,*], Gaoliang Dai[a], Sibylle Sievers[a], Alexander Fernández-Scarioni[a], Héctor Corte-León[b], Robert Puttock[b], Craig Barton[b], Olga Kazakova[b], Michal Ulvr[c,*], Petr Klapetek[c], Marek Havlíček[c], David Nečas[d], Yuanjun Tang[e], Volker Neu[e], Hans Werner Schumacher[a]

[a] Physikalisch-Technische Bundesanstalt (PTB), Braunschweig, Germany
[b] National Physical Laboratory (NPL), Teddington TW11 0LW, United Kingdom
[c] Czech Metrology Institute, Brno 638 00, Czech Republic
[d] Plasma Technologies, CEITEC, Masaryk University, Brno 62500, Czech Republic
[e] Leibniz IFW Dresden, Helmholtz Str. 20, Dresden, Germany

ARTICLE INFO

Keywords:
Comparison
Quantitative magnetic force microscopy
Magnetic probe calibration
Reference sample
Stray magnetic field

ABSTRACT

Magnetic force microscopy (MFM) can be considered as a standard tool for nano-scale investigation of magnetic domain structures by probing the local stray magnetic field landscape of the measured sample. However, this generally provides only qualitative data. To quantify the stray magnetic fields, the MFM system must be calibrated. To that end, a transfer function (TF) approach was proposed, that, unlike point probe models, fully considers the finite extent of the MFM tip. However, albeit being comprehensive, the TF approach is not yet well established, mainly due to the ambiguities concerning the input parameters and the measurement procedure. Additionally, the calibration process represents an ill-posed problem which requires a regularization that introduces further parameters. In this paper we propose a guideline for quantitative stray field measurements by standard MFM tools in ambient conditions. All steps of the measurement and calibration procedure are detailed, including reference sample and sample under test (SUT) measurements and the data analysis. The suitability of the reference sample used in the present work for calibrated measurements on a sub-micron scale is discussed. A specific regularization approach based on a Pseudo-Wiener Filter is applied and combined with criteria for the numerical determination of a unique regularization parameter. To demonstrate the robustness of such a defined approach, a round robin comparison of magnetic field measurements was conducted by four laboratories. The guideline, the reference sample and the results of the round robin are discussed.

1. Introduction

Local magnetic stray field measurements with a lateral resolution down to about 1 µm can be realized by various scanning probe techniques, such as Scanning Hall microscopy [1–3], scanning SQUID microscopy [4,5] and scanning MR magnetometry [6]. However, to achieve sub micrometer resolution, magnetic force microscopy is required, where lateral resolution can be as good as 10 nm when custom-made probes are used [7,8]. An ultimate (atomic) resolution is expected from the rapidly developing nitrogen-vacancy center microscopy [9]. Alternative to these scanning techniques, magneto-optical indicator film (MOIF) microscopy is a fast, parallel beam method with a resolution limit in the micrometer range. The calibration schemes for all these methods rely mostly on determining the sensor response to a homogeneous magnetic field. To obtain reliable calibrations with high spatial resolution, the influence of the response of the non-punctiform sensor in strongly spatially varying fields must be considered and needs to be implemented into the calibration procedures.

MFM can be considered as a standard tool for nano-scale investigations of magnetic nanostructures, thin films and devices with the benefit of high spatial resolution and ease of use [10]. MFM measurements only provide indirect measurements of spatially varying magnetic stray fields from the sample, therefore, leading to an ill-posed problem of the extraction of quantitative values. Furthermore, the measured signal strongly depends on the magnetic properties of the tip, the mechanical properties of the cantilever and the sensitivity of the

* Corresponding authors.
E-mail addresses: xiukun.hu@ptb.de (X. Hu), mulvr@cmi.cz (M. Ulvr).

https://doi.org/10.1016/j.jmmm.2020.166947
Received 6 January 2020; Received in revised form 24 April 2020; Accepted 24 April 2020
Available online 29 April 2020

detection device, which makes even reliable qualitative analysis a complex task. To quantitatively evaluate stray fields above a magnetic sample surface, the magnetic tip must firstly be calibrated by e.g. measuring current-carrying metal wires with very well-defined gradient of magnetic field [11–14], magnetic scanning gate microscopy [15], or measuring tip stray fields directly, e.g. through differential phase contrast in electron microscopy [16]. Alternatively, MFM measurements can be calibrated by quantifying their imaging performance on well-characterized magnetic reference samples. It results in a tip and instrument transfer function (TF) [17,18] that can be applied both, in real and Fourier space. The approach, which correctly considers the non-punctiform character of the magnetic tip, was proposed more than two decades ago [17]. Two different approaches have been developed for describing the so-called tip transfer function (TTF), using either the equivalent magnetic charge distribution in the tip apex plane [17–21] or the stray field gradient [22,23] of the tip. Both approaches are physically and mathematically equivalent. The TF is generally calibrated by a perpendicular-magnetized reference sample, and thin layer samples are used when it is required to reduce the stray field influence on the magnetic state of the used tips. This, however, requires an enhanced sensitivity of the MFM tool, such as provided by vacuum-based systems [8,19,20]. For the commonly used standard MFM tools in ambient conditions, the sensitivity is severely limited by thermal noise and cantilever damping, and thicker reference samples are used [22,23] to ensure sufficient signal-to-noise ratio. Despite the well-developed theory for TF characterization, no standardized implementation of the calibrated measurement process is available till now, leading to ambiguities and large uncertainties in the measured fields. Therefore, in this paper we propose a guideline for TF-based quantitative MFM measurements of nano-scale magnetic fields applicable for standard MFM instruments in ambient conditions. A round robin test between four laboratories has been carried out for the first time to verify the feasibility of such a guideline. The round robin test is detailed in the paper concerning the applied measurement procedures, data evaluation processes, the used reference samples, samples under test (SUT), measurement setups, and the results. Remaining issues are discussed.

2. Theory

2.1. MFM imaging process

In MFM a magnetic tip on an oscillating cantilever is scanned over an SUT at a constant tip-sample distance. The magnetic interaction between the tip and the sample leads to changes of the dynamic properties of the cantilever, which are typically measured as a phase shift between excitation and oscillation of the cantilever. This phase shift is proportional to the tip-sample force gradient for small oscillation amplitudes and phase shifts. Under the condition of a rigid tip magnetization [24] and non-perturbed sample magnetization, the MFM signal is a measure of the spatially varying magnetic stray field of the sample. This requires a careful selection of the used MFM tip with respect to the SUT, to avoid imaging artifacts or mutual (susceptibility) contrast – a procedure which is already important for a meaningful interpretation of qualitative images but even more important for a quantitative analysis of MFM data. The imaging process that leads to the MFM signal as a function of the sample stray field is thus governed by two processes: (i) the magnetic interaction of the spatially extended magnetic tip stray field with the spatially varying magnetic field of the SUT. This can be described as a correlation operation and leads to a force gradient acting on the oscillating cantilever. (ii) the conversion of the force gradient into a phase shift of the oscillating cantilever according to its mechanical properties. In two dimensional (2D) Fourier space, where the (x, y, z) space is mapped to the (k_x, k_y, z) space, the correlation becomes a multiplication and the following relation between the sample stray field $H_z^{sample}(\boldsymbol{k}, z)$ at a measurement height z above the sample surface and the MFM phase shift signal (in radian) at constant excitation frequency can be derived referring to [16–22].

Table 1
MFM key control parameters.

KCP	Description
z	measurement height
Q	cantilever quality factor
C	cantilever stiffness
s_x, s_y	image size in the x and y direction
n_x, n_y	pixel numbers
θ, φ	polar angle and azimuth angle describing normal orientation of the cantilever
A_0	cantilever oscillation amplitude

$$\Delta\phi(\boldsymbol{k}, z) = -\frac{2\mu_0 Q}{C} \bullet CF(\boldsymbol{k}, \theta, \varphi, A_0) H_z^{sample}(\boldsymbol{k}, z) \bullet \frac{\partial \hat{H}_z^{tip}(\boldsymbol{k}, z)}{\partial z} \tag{1}$$

Here, the hat marks the complex conjugate. $\frac{\partial H_z^{tip}(\boldsymbol{k},z)}{\partial z}$ is the effective stray field gradient of the tip in a plane parallel to the sample at the measurement height z (typically the position of the tip apex) and $\boldsymbol{k} = (k_x, k_y)$ the spatial wave vector in the measurement plane with $k = \sqrt{k_x^2 + k_y^2}$. The correction factor, $CF(\boldsymbol{k}, \theta, \varphi, A_0)$, accounts for the influences of the canting angles and the finite oscillation amplitude A_0 of the cantilever [21]. Following the derivation process as described in Ref. [21], it can be formulated as:

$$CF(\boldsymbol{k}, \theta, \varphi, A_0) = \left[\frac{a}{kA_0}\right]^2 \sum_{m=0}^{\infty} \frac{1}{m!(m+1)!}\left(\frac{a}{2}\right)^{2m} \tag{2}$$

where θ and φ are the polar and azimuth angles of the cantilever normal relative to the z- and x-axis, respectively, $a = A_0[k\cos\theta - i(k_x\cos\varphi\sin\theta + k_y\sin\varphi\sin\theta)]$, and $i = \sqrt{-1}$.

The measurement parameters which are needed for quantitative MFM according to Eq. (1) are summarized in Table 1 and are referred to as key control parameters, KCPs. These KCPs should either be measured or kept constant.

2.2. Regularized MFM setup calibration and calibrated field measurement

An MFM setup typically encompasses the used measuring instrument and the cantilever-tip ensemble. According to Eq. (1) a calibrated field measurement requires the calibration of the MFM setup, i.e. TF of the MFM setup referred to as $G(\boldsymbol{k}, z)$. It presents knowledge of the relation between the measured signal and the underlying field distribution $H_z^{sample}(\boldsymbol{k}, z)$ and is given by

$$G(\boldsymbol{k}, z) = -\frac{2\mu_0 Q}{C} \bullet CF(\boldsymbol{k}, \theta, \varphi, A_0) \bullet \frac{\partial \hat{H}_z^{tip}(\boldsymbol{k}, z)}{\partial z} \tag{3}$$

Thus,

$$\Delta\phi(\boldsymbol{k}, z) = \mathrm{G}(\boldsymbol{k}, z) \bullet H_z^{sample}(\boldsymbol{k}, z) \tag{4}$$

$\mathrm{G}(\boldsymbol{k}, z)$ can be further divided into purely magnetic contributions from the MFM tip and instrument dependent mechanical contributions:

$$\mathrm{G}(\boldsymbol{k}, z) = I(\boldsymbol{k}, \theta, \varphi, A_0, Q, C) \bullet \frac{\partial \hat{H}_z^{tip}(\boldsymbol{k}, z)}{\partial z} \tag{5}$$

with

$$I(\boldsymbol{k}, \theta, \varphi, A_0, Q, C) = -\frac{2\mu_0 Q}{C} \bullet CF(\boldsymbol{k}, \theta, \varphi, A_0) \tag{6}$$

$\frac{\partial H_z^{tip}(\boldsymbol{k},z)}{\partial z}$ is addressed as the tip transfer function, $TTF(\boldsymbol{k}, z)$, as used in Refs. [22,23]. It is one of several possible definitions of a TTF [18] and differs e.g. by a factor of $-k/2$ from the TTF used in Refs. [20,21], which is applied to the sample stray field gradient instead. Measuring the MFM signal $\Delta\phi^{ref}(\boldsymbol{k}, z)$ of a reference sample with a known field

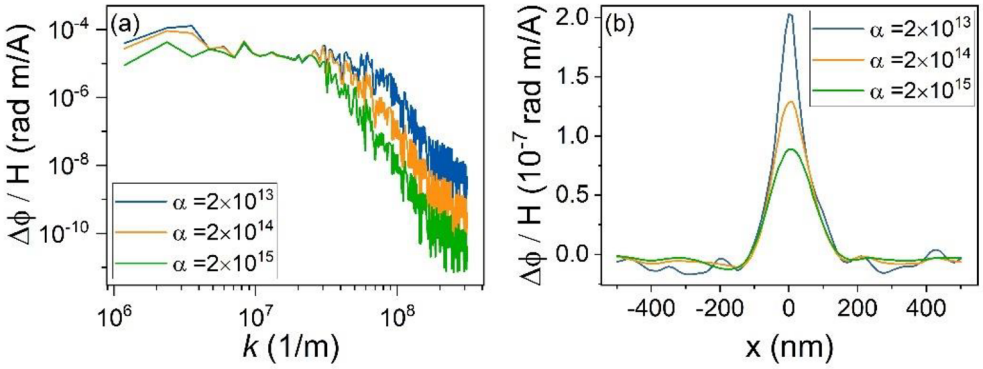

Fig. 1. Demonstration of the dependency of the MFM setup transfer function $G_\alpha(\boldsymbol{k}, z)$ on the regularization parameter α in real space (a) and in 2D Fourier space (b). Here, $\alpha = 2 \times 10^{14}$ is the optimized parameter.

distribution $H_z^{ref}(\boldsymbol{k}, z)$ in principal defines $G(\boldsymbol{k}, z)$. However, for real and inherently noisy MFM data the determination of the TF is an ill-posed problem and requires a regularization. The same holds for the determination of the stray field distribution $H^{SUT}(\boldsymbol{k}, z)$ of an SUT from a measurement with a characterized transfer function $G(\boldsymbol{k}, z)$.

2.2.1. Pseudo-Wiener filter approach for MFM setup calibration

For the MFM setup calibration based on a reference sample measurement with known $H_z^{ref}(\boldsymbol{k}, z)$, a pseudo-Wiener filter method [25] optimized for transfer function spectral properties is applied,

$$G_\alpha(\boldsymbol{k}, z) = \Delta\phi^{ref}(\boldsymbol{k}, z)\frac{\widehat{H}_z^{ref}(\boldsymbol{k}, z)}{|H_z^{ref}(\boldsymbol{k}, z)|^2 + \alpha} \tag{7}$$

where α is the regularization parameter. The choice of α is critical for the determination of TF and thus for the quantitative stray field measurements. In the TF calibration process α is determined by applying the so-called TTF width criterion [26], in which the width of the real space representation of the transfer function is minimized and evaluated on the area comparable to the expected width. To demonstrate the influence of α on TF, Fig. 1 shows three different $G(\boldsymbol{k}, z)$ in 2D fourier space (a) and in real space (b) calculated with different α. α of 2×10^{14} is the selected optimized regularizaiton parameter which gives a minimal TTF width (referred to Eq. (21) in [26]). It can be seen that a smaller α of 2×10^{13} makes the TF noisier (see e.g. high frequency contents in (a)) while a larger α of 2×10^{15} reduces the TF amplitude (both low and high frequency contents are despressed). This regularization method is applicable only for tip characterization, as the "TTF width" [26] is applied as the regularizaiton parameter selection criterion.

2.2.2. Pseudo-Wiener filter and L-Curve approach for calibrated field measurement

With a given TF, G ($\boldsymbol{k}$, z), the measured phase shift signal of the SUT can be transformed into quantitative stray field values. A Pseudo-Wiener filter approach is again pursued:

$$H_{\alpha'}^{SUT}(\boldsymbol{k}, z) = \Delta\phi^{SUT}(\boldsymbol{k}, z)\frac{\widehat{\mathrm{G}}(\boldsymbol{k}, z)}{|\mathrm{G}(\boldsymbol{k}, z)|^2 + \alpha'} \tag{8}$$

Here, another procedure, namely the L-curve criterion [27,28], is applied to determine an appropriate regularization parameter α'. In this procedure, each α' gives a pair of quantities: the 2-norms of the regularized solution $\|H_{\alpha'}^{SUT}(\boldsymbol{k}, z)\|_2$ and the corresponding residual $\|\Delta\phi^{SUT}(\boldsymbol{k}, z) - \mathrm{G}(\boldsymbol{k}, z)H_{\alpha'}^{SUT}(\boldsymbol{k}, z)\|_2$. These two quantities are plotted versus each other in log-log scale, showing an L-shaped convex curve. The optimized α' is extracted from the maximal curvature of the L-curve. The procedure is detailed in [27].

2.3. Stray field of perpendicularly magnetized samples

The MFM setup calibration requires a reference sample with known magnetic field distribution. We here use a thin film sample with perpendicular magnetic anisotropy (PMA) and stripe domain structure in the as-prepared, demagnetized state. The sample is assumed to be uniformly magnetized through its thickness. With known magnetic parameters, e.g., saturation magnetization M_S, domain wall width δ_{DW} etc., the stray field can be calculated from the surface magnetic charge distribution.

In general, the stray field of a magnetic layer with perpendicular magnetization distribution $(0, 0, M_z(x, y))$at a height z above the sample surface can be calculated in the 2D Fourier domain with 2D Fourier transform $M_z(x, y) \rightarrow M_z(k_x, k_y)$ [17,18]:

$$H_z^{ref}(k_x, k_y, z) = \frac{1}{2}M_z^{ref}(k_x, k_y)\bullet(1 - e^{-kd})\bullet e^{-kz} \tag{9}$$

Here, M_z^{ref} and d denote effective magnetization distribution and the magnetic layer thickness.

The stray field calculation procedure is illustrated in Fig. 2, where (a) shows a typical MFM image of a stripe domain sample. The magnetic parameters of the sample are described in Section 4.1. A phase profile marked by the line in Fig. 2(a) is plotted in Fig. 2(b) (magenta curve). After applying a discrimination process [18] by assuming equal integrated signals for up and down magnetized domains, the magnetization pattern denoted by $M_z^0(\pm M_S)$ was constructed as shown in Fig. 2(b) (red curve). To take into account the domain wall contribution, a convolution operation on the M_z^0 map with a kernel operator $f(x, y) = \mathrm{sech}^2\left(\frac{\pi\sqrt{x^2+y^2}}{\delta_{DW}}\right)$ for Bloch type domain wall [29] was performed. The result is shown as M_z^{ref} (green curve), which has smooth transition regions between adjacent domains. The H_z^{ref} data (blue curve) is then calculated by using Eq. (9). Replacing $H_z^{sample}(\boldsymbol{k}, z)$ in Eq. (1) by the obtained H_z^{ref} data and processing the data following the procedure as described in Section 2.2.1, the transfer function G ($\boldsymbol{k}$, z) can be calculated.

3. Measurement procedure and data evaluation

3.1. Assessing key control parameters

For a given MFM setup, TF consists of two components: $\frac{\partial\widehat{H}_z^{tip}(\boldsymbol{k}, z)}{\partial z}$ and $I(\boldsymbol{k}, \theta, \varphi, A_0, Q, C)$ as shown in Eq. (5). The component $\frac{\partial\widehat{H}_z^{tip}(\boldsymbol{k}, z)}{\partial z}$ is constant if the tip magnetic state is not influenced by SUTs. The component $I(\boldsymbol{k}, \theta, \varphi, A_0, Q, C)$ depends on KCPs as listed in Table 1. We denote such a component in the measurement of reference samples and of SUTs as $I^{ref}(\boldsymbol{k}, \theta, \varphi, A_0, Q, C)$ and $I^{SUT}(\boldsymbol{k}, \theta, \varphi, A_0, Q, C)$, respectively. To achieve I^{ref} and I^{SUT}, the KCPs need to be determined, as

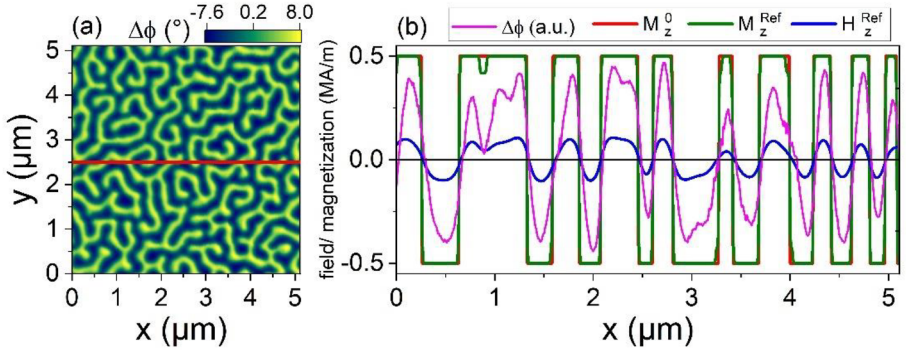

Fig. 2. Illustration of the stray field calculation process of the reference sample. (a) A typical MFM phase image of a reference sample with stripe domains. (b) The magenta curve shows the phase signal of the MFM image at the marked line in (a); The calculated domain pattern M_z^0, effective magnetization distribution M_z^{ref} and stray field are plotted as the red, green and blue curves, respectively. (For interpretation of the references to colour in this figure legend, the reader is referred to the web version of this article.)

described below:

- Cantilever stiffness C
  There are several standardized methods available for determining C: theoretical modeling based on the cantilever geometry [30], thermal noise spectrum method [31] or calibration using a reference spring with calibrated spring constant [32].
- Cantilever quality factor Q
  Q is typically obtained from the resonance curve of the cantilever as $Q = f_0/\Delta f$, where f_0 is the resonance frequency and Δf is the full bandwidth at 0.707 of the maximum amplitude [33]. Q is determined by the energy dissipation of the cantilever during oscillation, for instance, the squeeze-film air damping effect. In an MFM measurement, Q may vary significantly (ca. 20%) at different measurement heights (from 100 μm to 100 nm). However, from sample to sample, when using the same scanning parameters, the change due to scanning different surfaces is typically within 2%.
- Cantilever oscillation amplitude A_0
  Cantilever oscillation amplitude is the center-to-peak position of the oscillating cantilever. It can be traced to the atomic force microscope scanner motion via a force-distance curve obtained by monitoring the deflection of a cantilever with respect to the vertical displacement of the sample [34] when the tip is landed on a bare hard substrate (typically on a silicon substrate).
- Measurement height z
  The measurement height z is the distance between the sample surface and the average oscillation position of the tip apex. It is given as:

$$z = A_s + \text{lift height}$$

where, A_s is the oscillation amplitude setpoint of the tip when it contacts with the sample surface. The lift height is the distance increase when the tip lifts off the sample surface for magnetic signal imaging.

- Image sizes $s_x \times s_y$ and pixel numbers $n_x \times n_y$
  MFM images are scanned with equidistant pixel in the x- and y-directions.
- Cantilever normal orientation angles θ and φ
  The angles θ and φ are determined by the mechanical construction of the cantilever holder in an MFM tool and by the selected scanning orientation set by the user, respectively. They can be found in the instrument description.

In this study, we applied a same set of KCPs in both measurements on the reference sample and SUTs and assumed that I^{ref} and I^{SUT} are identical. The slight deviations of I^{ref} and I^{SUT} are considered as a part of measurement uncertainty, which is about 5%.

3.2. Measurement procedure

The measurement procedure comprises two parts – calibration of the magnetic tip and measurements with the calibrated tip on the selected locations of SUTs. It is performed in the following steps:

- Selection of suitable magnetic tips. Magnetization configurations of used tips and measured samples should not be affected by each other's stray fields. Hence, tips are chosen for their ability to create reproducible MFM images without obvious disturbances. The more subtle susceptibility contrast is excluded from consistency tests (see details in Section 4.1).
- Acquisition of the KCPs according to Section 3.1.
- Measurement of the reference sample for the tip calibration with well-adjusted measurement height z, giving data sets $\Delta\phi^{ref}$. Repeated measurements are recommended provided that tip wear remains negligible, e.g. in one passage MFM mode.
- Measurement of specified areas of the SUTs with identical KCPs and the same magnetic tip.
- Measurement of the reference sample for the tip calibration with identical parameters and the same magnetic tip, giving data sets $\Delta\phi^{ref}$.

3.3. Data analysis procedure

After the measurement, data are processed in order to calibrate the tip and evaluate the stray fields. The data processing procedure consists of the following steps:

- All phase data are inspected and corrected for potential errors (e.g. misalignment of the measured area on the samples).
- The stray field of the reference sample H_z^{ref} is calculated from the MFM data $\Delta\phi^{ref}$ as discussed in Section 2.3.
- G ($\boldsymbol{k}$, z) of the MFM setup is obtained by applying a pseudo-Wiener filter approach as discussed in Section 2.2.1. Only when TFs measured before and after the SUT agreed to within 10%, the measurements are regarded as reliable. When repeated MFM measurements are performed for TF calibration, the TFs should be averaged for noise reduction. In the case of obvious tip degradation, the measurement procedure was repeated with a new tip.
- A pseudo-Wiener filter and the L-curve method as discussed in Section 2.2.2 is performed to obtain the calibrated stray field results H_z^{SUT} of the SUT at the height z above the sample surface from the measured $\Delta\phi^{SUT}$ data and the previously derived transfer function G ($\boldsymbol{k}$, z).

4. Samples

4.1. Reference sample for tip calibration

A Co/Pt multilayer sample was used as a calibration sample (S0) for MFM measurements. The benefit of this type of sample is that it shows stable well-known magnetic properties and well-defined perpendicular stripe domains.

The multilayers were prepared by magnetron sputtering with the layer architecture Pt(2 nm)/[(Co(0.4 nm)/Pt(0.9 nm)]$_{100}$/Pt(5 nm)/Ta (5 nm)/SiO_x/Si(1 0 0) [22]. The total thickness of the magnetic layer is 130 nm. The film develops a magnetic anisotropy perpendicular to the surface due to the interface anisotropy. At zero-field the magnetization of the multilayer collapses into a stripe domain pattern with an average domain width of about 170 nm as shown in Fig. 2(a). Global magnetization measurements determine the saturation magnetization to be M_s = (500 ± 30) kA/m and confirm the perpendicular magnetization through a ratio $Q_u = K_u/K_d = 2.5$ (K_u = 0.4 MJ/m^3 is the perpendicular anisotropy constant, K_d = ½ $\mu_0 M_s^2$ = 0.16 MJ/m^3 is the magnetostatic energy density). The Bloch type domain transition has a widthδ_{DW} of approximately 16 nm.

The average domain width of about 170 nm and the even smaller features of the domain walls provide a stray field landscape with strong signal in the spatial frequency range from the image size down to some 10 nm. In our previous studies [22,35], we have verified a negligible mutual interaction between the reference sample and the used tips (team nanotech ML3 [22] and Nanosensors PPP-MFMR [35]) by performing a consistency check. That is, measured MFM images at different heights were compared with images calculated theoretically from the MFM image at the lowest height by the known experimental decay of the MFM signal in Fourier space, as suggested in [18,22]. Such a sample is thus used for the TF calibration, and the calibrated tip will reliably quantify unknown domain patterns of comparable spatial frequencies.

For tip calibration measurements specifying the measurement region is not necessary, since the above-mentioned stripe domain pattern develops homogeneously over the whole sample surface. Nevertheless, the measurement position was specified by coordinates with respect to a sample corner. The measured area $s_x \times s_y$ was chosen as 5.11 μm × 5.11 μm with 512 × 512 pixels.

4.2. SUTs for quantitative stray field measurement

Two samples (unstructured $SmCo_5$ thin film (S1) and patterned Co/Pt multilayer (S2)) were chosen as samples under test for calibrated stray field measurements. For the SUT measurements on S1 and S2, three measured areas were chosen with a scan size of 5.11 μm × 5.11 μm with 512 × 512 pixels.

The sample S1 is an epitaxially grown film of the hexagonal $SmCo_5$ phase, with c-axis orientation normal to the film plane. The film was prepared at IFW by UHV pulsed laser deposition (PLD) on a heated (650 °C) Ru-buffered Al_2O_3 substrate. The full layer architecture is Ta (3 nm)/$SmCo_5$(12 nm)/Ru(9 nm)/Al_2O_3(0001) and the epitaxial relation is < 11–20 > (0001)$SmCo_5$|| < 11–20 > (0001) Ru|| < 10–10 > (0001)Al_2O_3 [36]. Due to the large uniaxial magnetocrystalline anisotropy of the $SmCo_5$ phase with easy magnetization direction along the *z*-axis, the film develops strong PMA. The saturation magnetization is determined to be M_s = (660 ± 40) kA/m, and domain transition has a widthδ_{DW} of approximately 3 nm. In the as-prepared state, the sample shows patchy domains with individual domains normal to the sample surface. The domain size ranges from about 1 μm down to 100 nm. An example MFM image of the sample S1 is shown in Fig. 3(a).

The thin Co/Pt sample S2 has been prepared at IFW by magnetron sputtering. The layer architecture is Pt(2 nm)/[(Co(0.53 nm)/Pt (1.32 nm)]$_{10}$/Pt(5 nm) Ta(15 nm)/SiO_x/Si(1 0 0) and the total thickness of the magnetic layer is 18.6 nm. The saturation moment per unit area is determined by m_s/area = (1.04 ± 0.1) × 10^{-4} A, corresponding to a saturation magnetization of M_s = (560 ± 55) kA/m. Due to the interface anisotropy at the Co/Pt interfaces the multilayer develops a PMA with a magnetization direction within individual domains normal to the sample surface. Due to the low film thickness, the sample possesses domains of several micrometer in size, separated by easily movable domain walls susceptible to the scanning magnetic tip. In order to avoid domain wall movements in this sample, the multilayer has been patterned by e-beam lithography and argon etching into randomly arranged rectangular structures with sizes ranging from 2 μm down to 250 nm, small enough to maintain a fully magnetized state after saturation. Fig. 3(b) shows a topography of the pattern structure. The reddish regions correspond to the magnetic material and amount to 50% of the area. Magnetic material regions have a height of about 50 nm. The MFM image of this patterned sample is shown in Fig. 3(c).

The mutual influence between the MFM tip and the SUTs can also be neglected. Firstly, the magnetic stray field of both SUTs is weaker than that of the reference sample. Thus, its influence on the tip magnetization is even smaller. Secondly, both SUTs are characterized by an appreciable coercivity. In sample S1 the large coercivity (> 0.5 T) is a result of the highly anisotropic $SmCo_5$ phase; in S2 the single domain state is enforced by the confinement of the pattern structure. The SUT's magnetization state is thus not easy to be changed by the tip. As a result, the above sketched TF approach is applicable.

5. Round robin comparison

5.1. Description of the measurements

To demonstrate the robustness of the calibration and calibrated field measurements when following the approach as discussed above, a round robin comparison of magnetic stray field measurements was conducted by four participants (CMI: Czech Metrology Institute, Czech Republic; PTB: Physikalisch-Technische Bundesanstalt, Germany; IFW: Institute for Solid State and Material Research Dresden, Germany; and NPL: National Physical Laboratory, UK). The comparison was carried out by a circulation scheme. Three samples as described in Chapter 4 were sent to the participants in turn. The participants were required to perform the measurements with the following strategy: 1) MFM measurement of S0 at the recommended position. 2) MFM measurements of S1 and S2 at three specified positions (Pos. 1, Pos. 2 and Pos. 3). 3) Repeat the step 1. Each participant chooses the MFM probe from its own laboratory considering that the calibrated stray fields are traceable to the reference sample S0 and should be independent on the used tip. The Measurement setups of each participant and the KCPs are summarized in Table 2.

The measurements were performed following the approach discussed in Sections 3.2 and 3.3. The raw data from each participant were evaluated by the pilot laboratory using Gwyddion open source software [37] to ensure a laboratory independent choice of parameters during the data processing from phase shift signals to the measurements results.

5.2. Comparison results

Fig. 4 shows the MFM phase images (a-d) and the calibrated stray field maps (f-i) of the sample S1 measured at specified Pos. 2 by four participants. The magnetic domain structure is well captured by participants 1–3. Unfortunately, participant 4 could not perform the MFM measurement at the specified position. To compare the calibrated stray fields with the calculated ones, the effective magnetization pattern M_z was first constructed from Fig. 4(c) by using the known magnetic parameters of S1 as given in Section 4.2 and is displayed in Fig. 4(e). The stray field at *z* of 60 nm is then calculated using Eq. (9) and is given in Fig. 4(j). All H_z^{SUT}profiles marked by the dotted lines in Fig. 4(f-h) and (j) are compared and shown in Fig. 4(k). The overall stray field landscape captured by the participants 1–3 is in a good agreement with the calculated one. The measurement results of S1 at the other two specified positions are shown in Appendix (see Figs. A.1 and A.2). Since

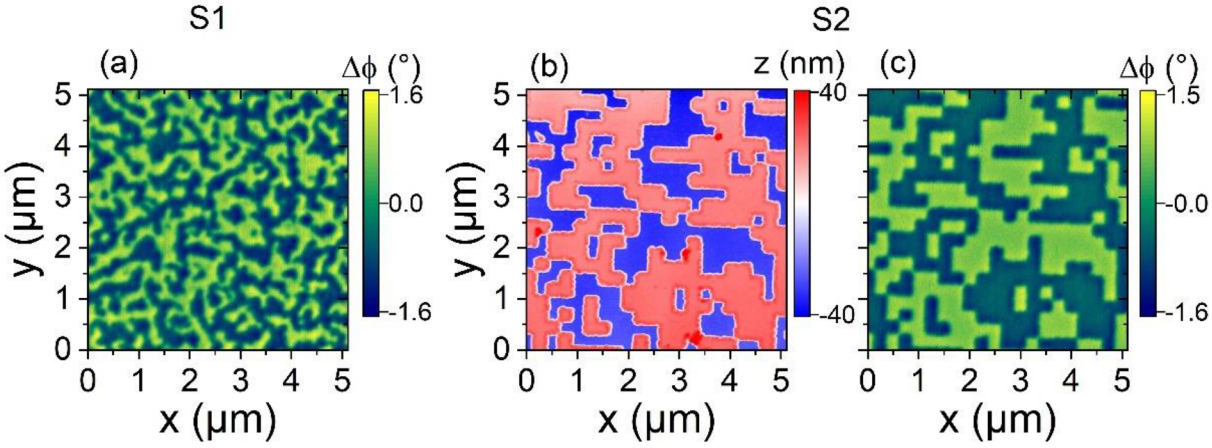

Fig. 3. (a) MFM image of $SmCo_5$ sample S1 in the as-prepared state. (b) A topography image of pattern Co/Pt sample S2. Red and blue colours denote the regions with magnetic materials and nonmagnetic trenches, respectively. (c) MFM image of such a patterned structure after saturation in the *z* direction. (For interpretation of the references to colour in this figure legend, the reader is referred to the web version of this article.)

the participant 4 did not measure the specified positions, only the results of the participants 1–3 were taken for the round robin comparison.

Fig. 5 shows the MFM phase images (a-d) and the calibrated stray field results (f-i) of the 4 different participants on S2 taken at nominally identical Pos. 2. The domain structure of the patterned sample was well imaged by the participants 1–3. The image captured by the participant 4 was measured at a different position and shows large signal spikes at the pattern edges. It is thus not taken for the round robin comparison. The pattern layout was used for constructing effective magnetization pattern M_z as shown in Fig. 5(e). The calculated H_z^{SUT} maps are shown in Fig. 5(j). Calibrated H_z^{SUT} profiles as denoted by the dotted lines in Fig. 5(f-h) together with the calculated one in Fig. 5(j) are compared in Fig. 5(k). Again, the overall corrugation of the stray field landscape is well captured by all measurements. The measurement results of S2 at the other two specified positions are shown in Appendix (see Figs. A.3 and A.4). Switching of single domains was observed in the images measured by one laboratory at Pos. 1 and Pos. 3 as indicated by white arrows in Figs. A.3 and A.4, respectively. The measurements on these positions are thus not taken for the round robin comparison.

The effective quantitative measurements of S1 and S2 show a good overall agreement of the stray field landscapes among three participants, as displayed in Figs. 4(k) and 5(k). However, there are obvious differences between the individual profiles, which are attributed mainly to the positioning inaccuracy. To compare the values of the whole map point by point requires a spatial alignment procedure, which, however, cannot be performed with nanometer precision. Therefore, the root mean square value of the stray fields, Hz_{rms}, of the calibrated measurements were used for the round robin comparison.

The calibrated Hz_{rms} data for three different positions (Pos.1, Pos.2 and Pos.3) on S1 and for the Pos.2 on S2 were compared in Fig. 6(a) and (b), respectively. Due to the homogeneity of the domain pattern within S1, measurements on different positions are expected to give similar results, as it is observed in the calibrated data. The differences of the measured Hz_{rms} among the different participants are smaller than 25% for S1 and 20% for S2 as it is shown in Fig. 6. It is worth mentioning that Hz_{rms} values of the measurements at three different positions by participant 4 are calculated as 14.92, 14.78, and 16.56 kA/m, respectively. They are comparable with the results from other participants, confirming that the sample exhibits a good homogeneity of the domain pattern.

For the comparison, the uncertainties were evaluated according to [27]. The standard uncertainty values are in the range of 15–18% for S1 and 14–17% for S2. For all measurements, the evaluation of this comparison was performed following the procedure A in [38]. Based on the Hz_{rms} data and their uncertainties from all participants the following characteristics were calculated: a reference value $x_{ref} = \sum_{i=1}^{N} x_i/u^2(x_i)/[\sum_{i=1}^{N} 1/u^2(x_i)]$, standard uncertainty of the reference value of stray field $u(x_{ref}) = \sqrt{1/[\sum_{i=1}^{N} 1/u^2(x_i)]}$ and the degree of equivalence of the measurement standard $d_i = x_i - x_{Ref}$ with a corresponding uncertainty $u(d_i) = \sqrt{u^2(x_i) - u^2(x_{ref})}$. Finally, a factor E_n was calculated according to

$$E_n = \frac{|d_i|}{2u(d_i)} \tag{10}$$

The consistency between the labs is judged as confirmed if the equation $|E_n| < 1$ is satisfied. The calculated values of E_n are presented in Fig. 7(a) and (b).

6. Discussion

The round robin test shows a good consistency of the measurement

Table 2
Description of the measurement setups.

Participant		CMI	PTB	IFW	NPL
MFM setup information	Instrument	Bruker Dimension Icon system	Self-developed metrological large-range MFM [35]	Bruker Dimension Icon system	Bruker Dimension Icon system
	Tip type	Nanosensors PPP-MFMR			
	Scan rate (μm/s)	5	10	5	5, 10
KCPs	C (N/m)	9.1	3.8	3.4	2.2
	Q	219	243–248	230	221
	$s_x \times s_y$, $n_x \times n_y$	5.11 μm × 5.11 μm, 512 × 512 pixels			
	θ, φ (°)	12, 180	7, 0	8, 180	8, 180
	A_0 (nm)	20	20	30	20
	z (nm)	60			

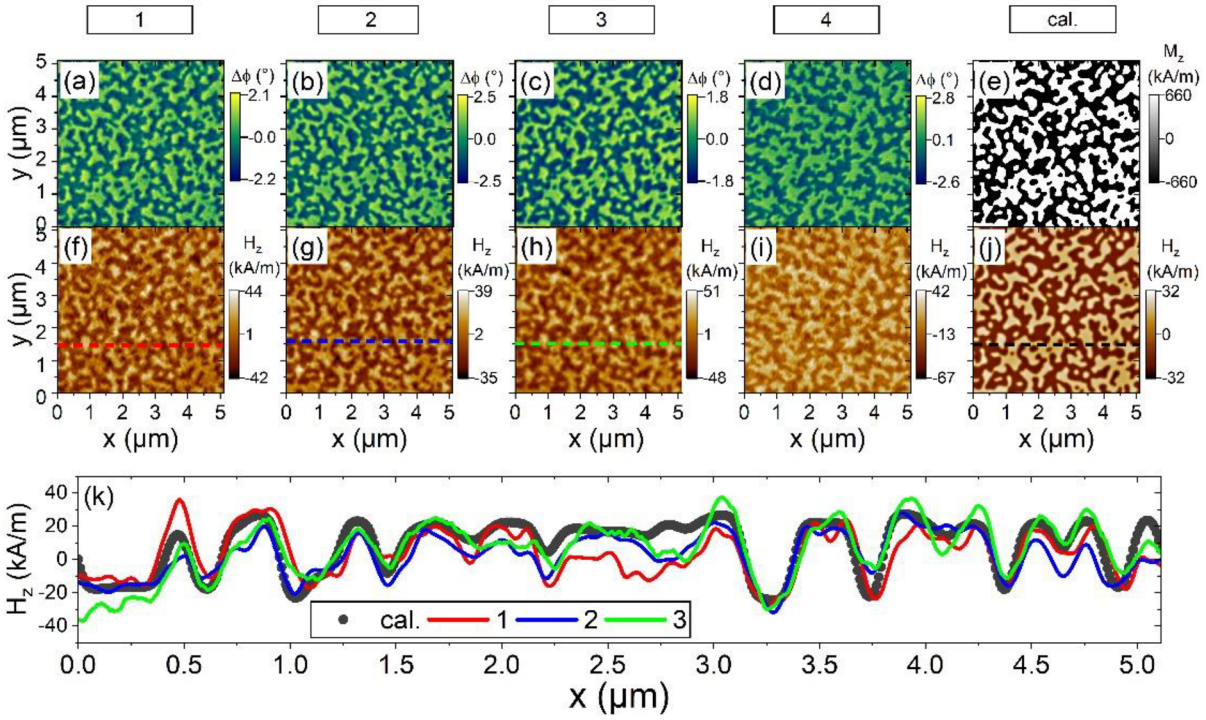

Fig. 4. Results of the sample S1 at Pos. 2 measured by 4 participants: (a-d) MFM images. (f-i) Calibrated H_z maps. (e) The effective magnetization pattern M_z after applying a discrimination process for (c). (j) The calculated stray field at z = 60 nm from (e) according to Eq. (9). (k) Profiles of H_z taken from the dotted lines in (f-h) and (j).

results among three different labs. However, several problems were identified during the round robin comparison by different partners, which might serve to improve the measurement and data analysis protocol in the future: 1) Switching of the tip magnetization when measuring S0 was observed in some cases. Measurements had thus to be repeated with a different probe. Moreover, single domain structures were disturbed or totally switched by an oppositely magnetized tip in some test measurements, (see Figs. A.3-A.4 in Appendix). It indicates that the mutual influence between the tip and the sample needs to be further studied. 2) Finding the specified area locations on millimetre-

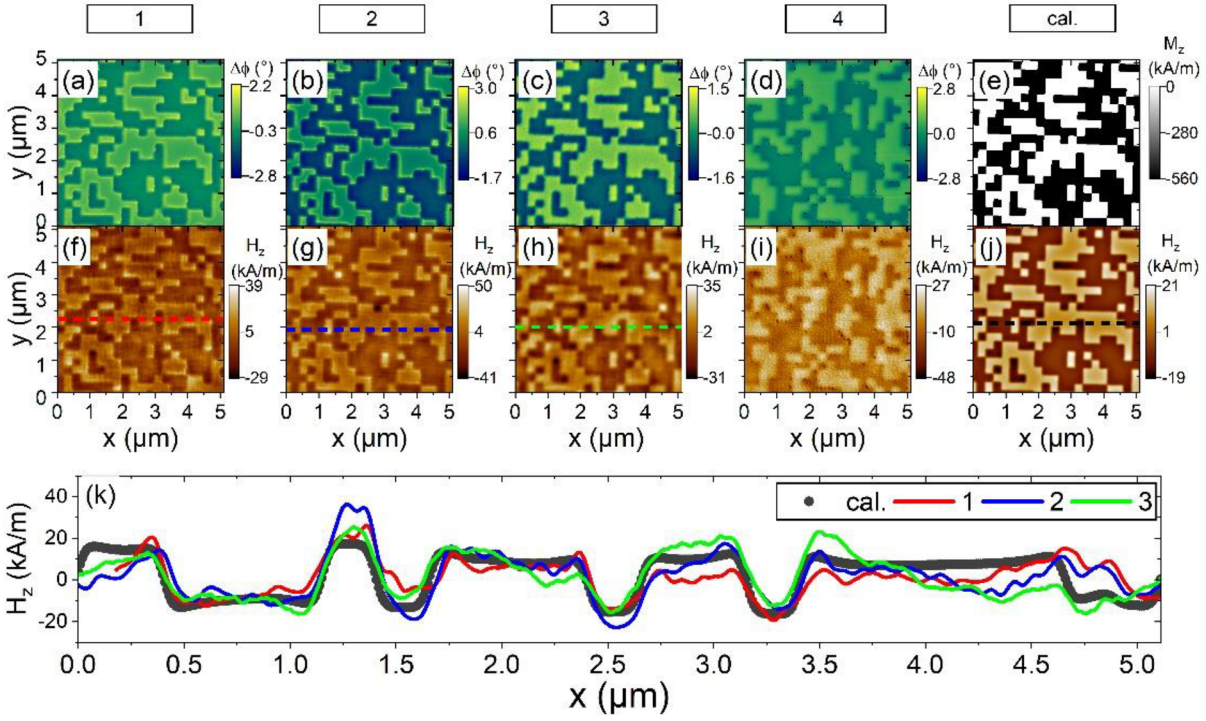

Fig. 5. Results of the sample S2 at Pos. 2 measured by 4 participants: (a-d) MFM images. (f-i) Calibrated H_z maps. (e) The effective magnetization pattern M_z. Black regions represent the patterned single magnetic domain. (j) The calculated stray field at z = 60 nm from (e) according to Eq. (9). (k) Profiles of H_z taken from the dotted lines in (f-h) and (j).

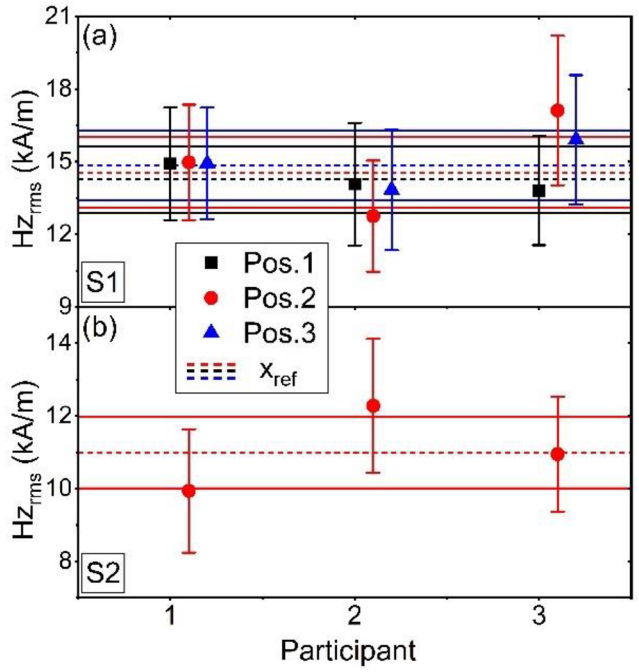

Fig. 6. Comparison results of calibrated stray magnetic field Hz_{rms} of thin SmCo sample S1 at three specified positions (a) and of thin Co/Pt sample S2 at the specified position 2 (b) by three participants. The dashed lines denote the reference values of stray field (x_{ref}) at different measured positions. The horizontal solid lines represent the standard uncertainty of x_{ref}.

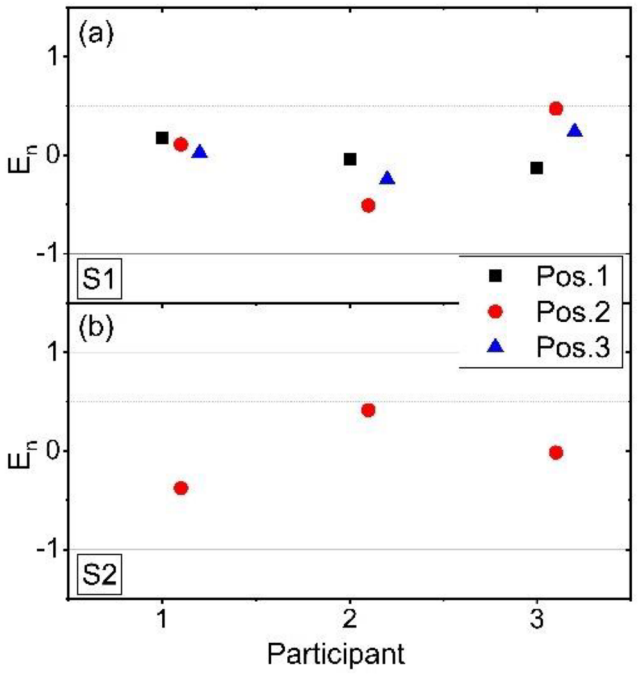

Fig. 7. Results of calculated factor E_n of SmCo sample S1(a) and Co/Pt sample S2(b).

scale samples by a magnetic tip was problematic for one partner. The tip might become blunt or the magnetic coating destroyed when several scans on the sample surface are needed before finding the specified position. A pre-characterization with a non-calibrated tip prior to the quantitative measurement procedure will help. 3) The comparison with independent analysis techniques for the stray field by individual partners (not shown here) underlined the importance of well defining the parameters of the deconvolution procedure for tip transfer function estimation and for the stray field evaluation. In particular, the treatment of the higher spatial frequencies in the tip transfer function was found to have significant impact on the measured fields. To avoid these additional sources of deviations, the analysis was performed by the pilot laboratory in the identical way for all participants. However, the calibrated stray field of SUTs show noisier signal than the calculated one (see Figs. 4(k) and 5(k)), indicating that the regularization process needs to be further studied and optimized.

7. Conclusions

In this paper, we presented detailed implementation of quantitative MFM for measuring nanoscale magnetic stray field based on a transfer function approach. Step-by-step instructions of the measurement and calibration procedure are described, including the collection of the key control parameters, the selection of a suitable reference sample, detailed measurement procedures and the data analysis procedure. A round robin comparison of calibrated MFM measurements between four labs, CMI, PTB, IFW, and NPL has been presented. The results of three participating labs were compared, showing a good consistency of measured stray field values, independent on the tips, equipment and operator. This proves the robustness of the described transfer function approach when the detailed measurement procedure as described above is followed. The remaining issues have been discussed for further improving the measurement and data analysis protocol. The results support the establishment of a standardized method for quantitative nanometer scale stray field measurement by standard magnetic force microscopy in ambient conditions.

CRediT authorship contribution statement

Xiukun Hu: Writing - original draft, Methodology, Investigation. **Gaoliang Dai:** Methodology, Investigation. **Sibylle Sievers:** Writing - original draft, Methodology, Investigation. **Alexander Fernández-Scarioni:** Methodology. **Héctor Corte-León:** Writing - original draft, Methodology, Investigation. **Robert Puttock:** Investigation. **Craig Barton:** Investigation. **Olga Kazakova:** Investigation. **Michal Ulvr:** Formal analysis, Supervision. **Petr Klapetek:** Writing - original draft, Software, Investigation. **Marek Havlíček:** Methodology, Investigation, Formal analysis, Data curation. **David Nečas:** Software, Data curation. **Yuanjun Tang:** Investigation. **Volker Neu:** Methodology, Writing - original draft, Investigation. **Hans Werner Schumacher:** Project administration, Supervision.

Declaration of Competing Interest

The authors declare that they have no known competing financial interests or personal relationships that could have appeared to influence the work reported in this paper.

Acknowledgements

This work was supported by joint research project 15SIB06 'NanoMag' in the EMPIR program co-financed by the Euramet participating states, European Union's Horizon 2020 programme and European Regional Development Fund-Project 'CEITEC Nano+' (No. CZ.02.1.01/0.0/0.0/16_013/0001728). We acknowledge C. Krien for preparing the Co/Pt multilayers.

Appendix

Quantitative MFM results obtained at Pos. 1 and Pos. 3 of sample S1 and S2 are shown below:

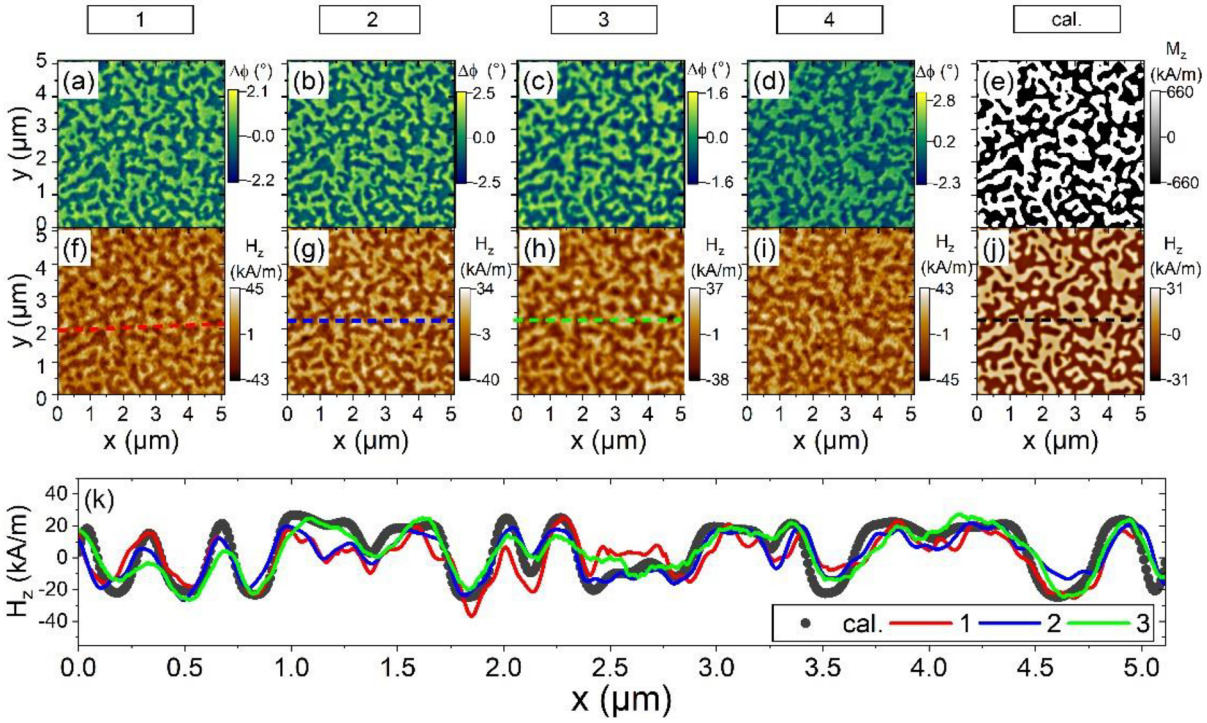

Fig. A1. Results of the sample S1 at Pos. 1 measured by 4 participants: (a-d) MFM images. (f-i) Calibrated H_z maps. (e) The effective magnetization pattern M_z after applying a discrimination process to (c). (j) The calculated H_z at $z = 60$ nm from (e) according to Eq. (9). (k) Profiles of H_z taken from the dotted lines in (f-h) and (j). The red curve is shifted to align the position with other profiles.

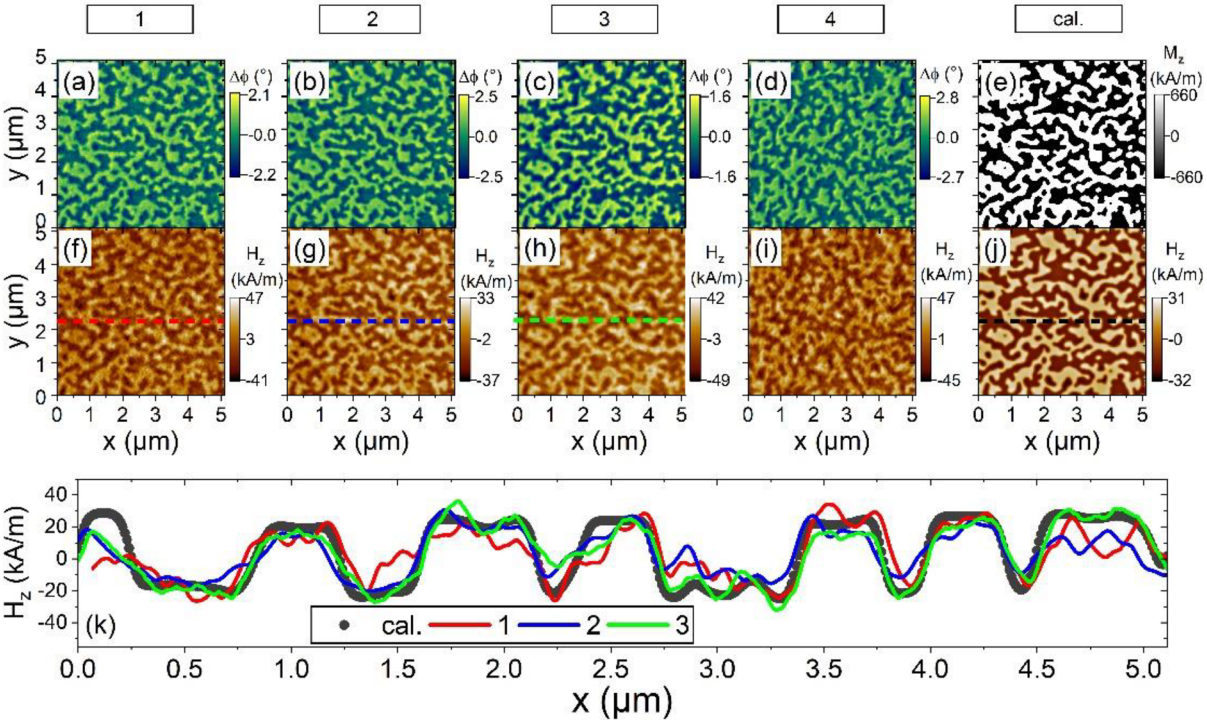

Fig. A2. Results of the sample S1 at Pos. 3 measured by 4 participants: (a-d) MFM images. (f-i) Calibrated H_z maps. (e) The effective magnetization pattern M_z after applying a discrimination process to (c). (j) The calculated H_z at $z = 60$ nm from (e) according to Eq. (9). (k) Profiles of H_z taken from the dotted lines in (f-h) and (j).

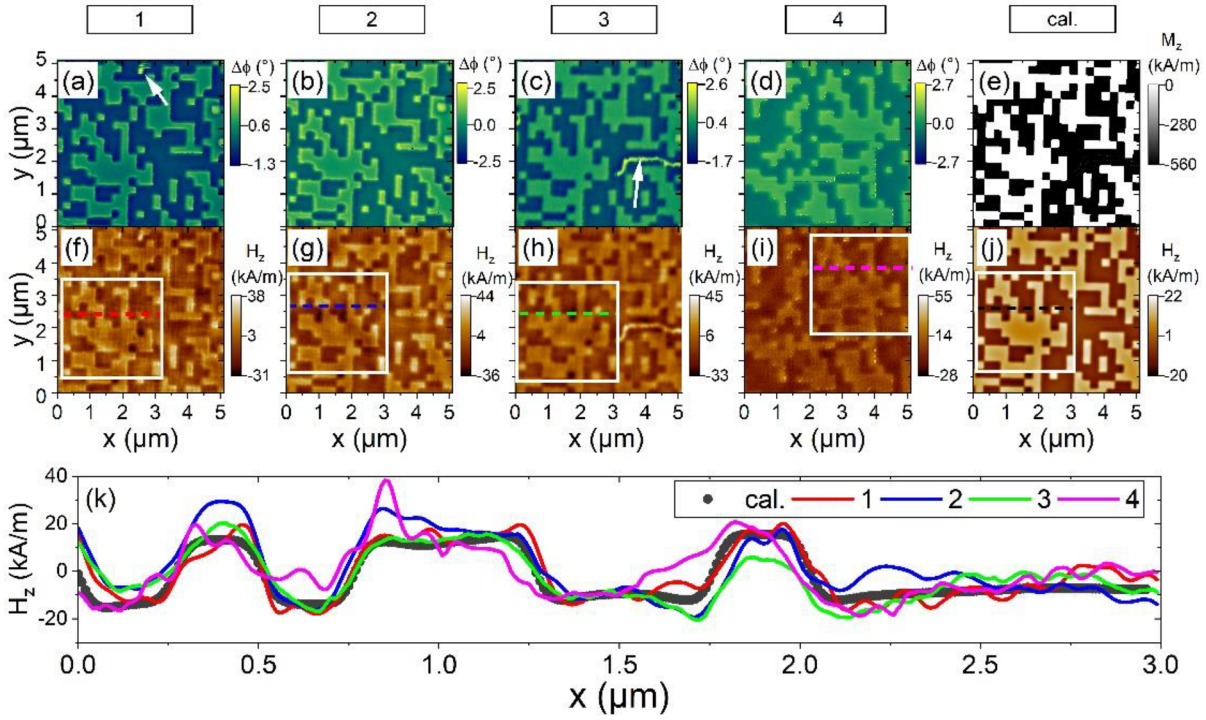

Fig. A3. Results of the sample S2 measured at Pos. 1 measured by 4 participants: (a-d) MFM images. (f-i) Calibrated H_z maps. (e) The effective magnetization pattern M_z. Black regions represent the patterned single magnetic domain. (j) The calculated H_z at $z = 60$ nm from (e) according to Eq. (9). White boxes in (f-j) mark the overlapped measured region of 4 participants. (k) Profiles of H_z taken from the dotted lines in (f-j). White arrows mark reversed domains induced by the magnetic tip during the test measurements.

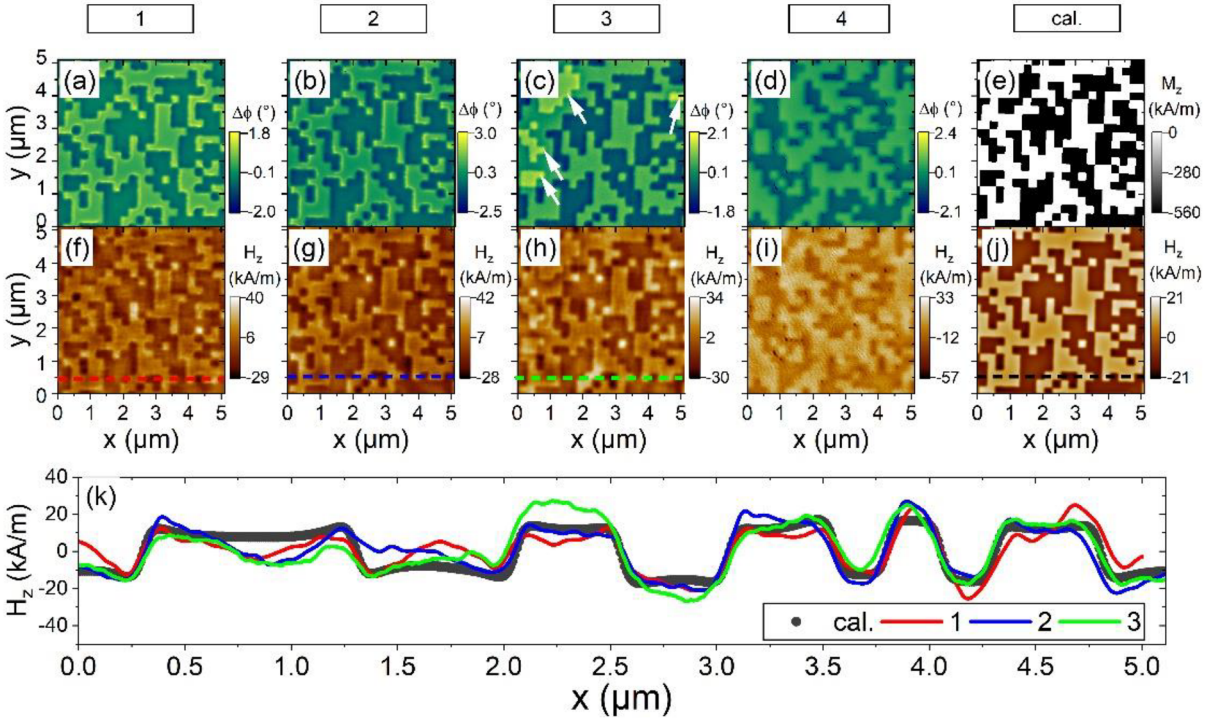

Fig. A4. Results of the sample S2 measured at Pos. 3 measured by 4 participants: (a-d) MFM images. (f-i) Calibrated H_z maps. (e) The effective magnetization pattern M_z. Black regions represent the patterned single magnetic domain. (j) The calculated H_z at $z = 60$ nm from (e) according to Eq. (9). (k) Profiles of H_z taken from the dotted lines in in (f-h) and (j). White arrows mark reversed domains induced by the magnetic tip during the test measurements.

References

[1] G. Shaw, R.B.G. Kramer, N.M. Dempsey, K. Hasselbach, A scanning Hall probe microscope for high resolution, large area, variable height magnetic field imaging, Rev. Sci. Instrum. 87 (2016) 113702.

[2] C. Xue, J.-Y. Ge, A. He, V.S. Zharinov, V.V. Moshchalkov, Y.H. Zhou, A.V. Silhanek, J. Van de Vondel, Mapping degenerate vortex states in a kagome lattice of elongated antidots via scanning Hall probe microscopy, Phys. Rev. B 96 (2017) 024510.

[3] E. Marchiori, S.J. Bending, Mapping the flux penetration profile in a 2G-HTS tape at the microscopic scale: deviations from a classical critical state model, Supercond. Sci. Technol. 32 (2019) 025009.

[4] A. Finkler, Y. Segev, Y. Myasoedov, M.L. Rappaport, L. Ne'eman, D. Vasyukov, E. Zeldov, M.E. Huber, J. Martin, A. Yacoby, Self-aligned nanoscale SQUID on a tip, Nano Lett. 10 (2010) 1046–1049.

[5] L. Bishop-Van Horn, Z. Cui, J.R. Kirtley, K.A. Moler, Cryogen-free variable temperature scanning SQUID microscopy, Rev. Sci. Instrum. 90 (2019) 063705.

[6] D. Mitin, M. Grobis, M. Albrecht, Scanning magnetoresistive microscopy: an advanced characterization tool for magnetic nanosystems, Rev. Sci. Instrum. 87 (2016) 023703.

[7] X. Zhao, J. Schwenk, A.O. Mandru, M. Penedo, M. Baćani, M.A. Marioni, H.J. Hug, Magnetic force miscroscopy with frequency-modulated capacitive tip-sample distance control, New J. Phys. 20 (2018) 013018.

[8] K.Y. Meng, A.S. Ahmed, M. Baćani, A.O. Mandru, X. Zhao, N.B. Salguero, B.D. Esser, J. Flores, D.W. McComb, H.J. Hug, F. Yang, Observation of nanoscale skyrmions in $SrIrO_3$/$SrRuO_3$ Bilayers, Nano Lett. 19 (2019) 3169–3175.

[9] R. Schirhagl, K. Chang, M. Loretz, C.L. Degen, Nitrogen-vacancy centers in diamond: nanoscale sensors for physics and biology, Annu. Rev. Phys. Chem. 65 (2014) 83–105.

[10] O. Kazakova, R. Puttock, C. Barton, H. Corte-León, M. Jaafar, V. Neu, A. Asenjo, Frontiers of magnetic force microscopy, J. Appl. Phys. 125 (2019) 060901.

[11] T. Göddenhenrich, H. Lemke, M. Mück, U. Hartmann, C. Heiden, Probe calibration in magnetic force microscopy, Appl. Phys. Lett. 57 (1990) 2612–2614.

[12] L. Kong, S.Y. Chou, Quantification of magnetic force microscopy using a micronscale current ring, Appl. Phys. Lett. 70 (1997) 2043–2045.

[13] Th. Kebe, A. Carl, Calibration of magnetic force microscopy tips by using nanoscale current-carrying parallel wires, J. Appl. Phys. 95 (2004) 775.

[14] H. Corte-León, V. Neu, A. Manzin, C. Barton, Y. Tang, M. Gerken, P. Klapetek, H.W. Schumacher, O. Kazakova, Comparison and validation of different magnetic force microscopy calibration schemes, Small 16 (2020) 1906144.

[15] V. Panchal, Ó. Iglesias-Freire, A. Lartsev, R. Yakimova, A. Asenjo, O. Kazakova, Magnetic scanning probe calibration using graphene Hall sensor, IEEE Trans. Magn. 49 (2013) 3520–3523.

[16] S. McVitie, R.P. Ferrier, J. Scott, G.S. White, A. Gallagher, Quantitative field measurements from magnetic force microscope tips and comparison with point and extended charge models, J. Appl. Phys. 89 (2001) 3656–3661.

[17] H.J. Hug, B. Stiefel, P.J.A. van Schendel, A. Moser, R. Hofer, S. Martin, H.-J. Güntherodt, S. Porthun, L. Abelmann, J.C. Lodder, G. Bochi, R.C. O'Handley, Quantitative magnetic force microscopy on perpendicularly magnetized samples, J. Appl. Phys. 83 (1998) 5609–5620.

[18] P.J.A. van Schendel, H.J. Hug, B. Stiefel, S. Martin, H.-J. Güntherodt, A method for the calibration of magnetic force microscopy tips, J. Appl. Phys. 88 (2000) 435–445.

[19] X. Zhao, A.-O. Mandru, C. Vogler, M.A. Marioni, D. Suess, H.J. Hug, Magnetization reversal of strongly exchange-coupled double nanolayers for spintronic devices, ACS Appl. Nano Mater. 2 (2019) 7478–7487.

[20] M. Baćani, M.A. Marioni, J. Schwenk, H.J. Hug, How to measure the local Dzyaloshinskii-Moriya interaction in skyrmion thin-film multilayers, Sci. Rep. 9 (2019) 3114.

[21] Johannes Schwenk, Multi-modal and quantitative magnetic force microscopy: application to thin film systems with interfacial Dzyaloshinskii-Moriya interaction, Ph. D thesis, Basel, 2016.

[22] S. Vock, C. Hengst, M. Wolf, K. Tschulik, M. Uhlemann, Z. Sasvári, D. Makarov, O.G. Schmidt, L. Schultz, V. Neu, Magnetic vortex observation in FeCo nanowires by quantitative magnetic force microscopy, Appl. Phys. Lett. 105 (2014) 172409.

[23] S. Vock, Z. Sasvári, C. Bran, F. Rhein, U. Wolff, N.S. Kiselev, A.N. Bogdanov, L. Schultz, O. Hellwig, V. Neu, Quantitative magnetic force microscopy study of the diameter evolution of bubble domains in a $(Co/Pd)_{80}$ multilayer, IEEE Trans. Magn. 47 (2011) 2352–2355.

[24] V. Neu, S. Vock, T. Sturm, L. Schultz, Epitaxial hard magnetic $SmCo_5$ MFM tips – a new approch to advanced magnetic force microscopy imaging, Nanoscale 10 (2018) 16881.

[25] N. Wiener, Extrapolation, interpolation and smoothing of stationary time series, with engineering applications, Eastford, CT, USA, Martino Fine Books, 2013.

[26] D. Nečas, P. Klapetek, V. Neu, M. Havlíček, R. Puttock, O. Kazakova, X. Hu, L. Zajíčková, Determination of tip transfer function for quantitative MFM using frequency domain filtering and least squares method, Sci. Rep. 9 (2019) 3880.

[27] X. Hu, G. Dai, S. Sievers, A. Fernández Scarioni, V. Neu, M. Bieler, H.W. Schumacher, Uncertainty analysis of stray field measurements by quantitative magnetic force microscopy, IEEE Trans. Instrum. Meas. (2020), https://doi.org/10.1109/TIM.2020.2986865.

[28] P.C. Hansen, The L-Curve and its use in the numerical treatment of inverse problems, in: P. Johnston (Ed.), Computational Inverse Problems in Electrocardiology, WIT, Southampto, 2001, pp. 119–142.

[29] M.D. DeJong, K.L. Livesey, Analytic theory for the switch from Bloch to Néel domain wall in nanowires with perpendicular anisotropy, Phys. Rev. B 92 (2015) 214420.

[30] O. Wolter, Th. Bayer, J. Greschner, Micromachined silicon sensors for scanning force microscopy, J. Vac. Sci. Technol. B 9 (1991) 1353–1357.

[31] S.M. Cook, T.E. Schäffer, K.M. Chynoweth, M. Wigton, R.W. Simmonds, K.M. Lang, Practical implementation of dynamic methods for measuring atomic force microscope cantilever spring constants, Nanotechnology 17 (2006) 2135–2145.

[32] S. Gao, U. Brand, S. Hahn, K. Hiller, An active reference spring array for in-situ calibration of the normal spring constant of AFM cantilevers, in SPIE 9517 Smart sensors, Actuators and MEMS VII; and Cyber Physical Systems, 2015, p. 951719.

[33] G. Meyer, N.M. Amer, Novel optical approach to atomic force microscopy, Appl. Phys. Lett. 53 (1988) 1045–1047.

[34] D. Sarid, Scanning Force Microscopy: With Applications to Electric, Magnetic and Atomic Forces, Oxford University Press, New York, 1994, p. 21.

[35] G. Dai, X. Hu, S. Sievers, A. Fernández Scarioni, V. Neu, J. Flügge, H.W. Schumacher, Metrological large range magnetic force microscopy, Rev. Sci. Instrum. 89 (2018) 093703.

[36] M. Seifert, V. Neu, L. Schultz, Epitaxial $SmCo_5$ thin films with perpendicular anisotropy, Appl. Phys. Lett. 94 (2009) 022501.

[37] D. Nečas, P. Klapetek, Gwyddion: an open-source software for SPM data analysis, Cent. Eur. J. Phys. 10 (2012) 181–188.

[38] W. Bich, M. Cox, T. Estler, L. Nielsen, W. Woeger, Draft for discussion: Proposed guidelines for the evaluation of key comparison data, https://www.bipm.org/cc/CCAUV/Allowed/3/CCAUV02-36.pdf, 2002.